Monitoring Early-Stage Nanoparticle Assembly in Microdroplets by Optical Spectroscopy and SERS

Andrew R. Salmon, Ruben Esteban, Richard W. Taylor, James T. Hugall, Clive A. Smith, Graeme Whyte, Oren A. Scherman, Javier Aizpurua, Chris Abell, and Jeremy J. Baumberg*

Microfluidic microdroplets have increasingly found application in biomolecular sensing as well as nanomaterials growth. More recently the synthesis of plasmonic nanostructures in microdroplets has led to surface-enhanced Raman spectroscopy (SERS)-based sensing applications. However, the study of nanoassembly in microdroplets has previously been hindered by the lack of on-chip characterization tools, particularly at early timescales. Enabled by a refractive index matching microdroplet formulation, dark-field spectroscopy is exploited to directly track the formation of nanometer-spaced gold nanoparticle assemblies in microdroplets. Measurements in flow provide millisecond time resolution through the assembly process, allowing identification of a regime where dimer formation dominates the dark-field scattering and SERS. Furthurmore, it is shown that small numbers of nanoparticles can be isolated in microdroplets, paving the way for simple high-yield assembly, isolation, and sorting of few nanoparticle structures.

1. Introduction

Surface-enhanced Raman spectroscopy (SERS) allows the vibrational scattering of molecules to be amplified by factors as large as 10 billion.[1] Such enhancements allow for single molecule detection,[2–4] and therefore substantial interest exists to develop practical, robust, and quantitative SERS-based sensing tools. SERS operates by confining light on the nanoscale using plasmonically active metal surfaces, typically in small gaps between gold or silver nanoparticles. The mechanism of SERS is intrinsically nanoscale and is extraordinarily sensitive to the morphology of the plasmonic nanostructure. This sensitivity implies that design, control, and detailed characterization of the metallic nanostructures

A. R. Salmon, Prof. O. A. Scherman, Prof. C. Abell
Department of Chemistry
University of Cambridge
Lensfield Rd, Cambridge CB2 1EW, UK

A. R. Salmon, Dr. R. W. Taylor, Dr. J. T. Hugall,
Prof. J. J. Baumberg
Department of Physics
University of Cambridge
Cavendish Laboratory
JJ Thompson Avenue
Cambridge CB3 0HE, UK
E-mail: jjb12@cam.ac.uk

Dr. R. Esteban, Prof. J. Aizpurua
Materials Physics Center (CSIC-UPV/EHU) and DIPC
Paseo Manuel de Lardizabal 4
Donostia-San Sebastian, ES 20018, Spain

Dr. J. T. Hugall
ICFO
The Barcelona Institute of Science and Technology
Barcelona 08860, Spain

Dr. C. A. Smith
Sphere Fluidics Limited
Babraham Research Campus
Cambridge CB22 3AT, UK

Dr. G. Whyte
Heriot-Watt University
School of Engineering and Physical Sciences
David Brewster Building
Edinburgh EH14 4AS, UK

are essential. Commonly, fluid processes are used to assemble the nanostructures as well as to introduce analytes into the active sensing volume between the nanoparticles, and are thus intrinsic to the spectroscopic control.

The rapid development of microfluidics offers precise control of fluids and so its application to SERS follows naturally.[5] There is particular interest in microdroplet-based SERS applications. For example, there has been work on tracking chemical reactions,[6] biological analysis and bacterial discrimination,[7,8] high speed measurements,[9,10] and much work on low-concentration analyte detection.[11–16] Microfluidic droplets are also increasingly used to create plasmonic structures as nanoparticle synthesis/assembly often relies on fast and controlled mixing that microdroplets can provide. Consequently, microdroplets have been used in nanoparticle synthesis[17,18] as well as for the creation of composite plasmonic structures.[19,20]

Microdroplets contain discrete monodisperse sample volumes (nanoliter to picoliter) that can be automatically manipulated in many ways (as drops can be mixed, fused, probed, sorted, etc.).[21,22] Hence, they provide an ideal platform to regulate the number of assembling nanoparticles under highly controlled conditions. However, a key limiting factor to current microfluidics is the restricted range of on-chip characterization and analysis tools.[23] Microdroplet microfluidics and SERS are thus complementary, since microdroplets provide fluidic control for SERS, while SERS provides a method amenable to multiplex sensing in an environment where it is otherwise difficult to integrate probes.

Despite the substantial interest in integrating SERS-based sensing with microdroplet microfluidics, nanostructure plasmonics have been difficult to characterize and thus optimize in this environment. Broadly speaking, the SERS response is largest when the dominant plasmon mode is resonant near the laser excitation wavelength (normally one of a fixed set of laser lines). The sample can also restrict the usable laser wavelengths, for example, in biological applications where near-infrared lasers are preferred. Consequently, plasmon geometries must be modified to achieve resonance with a given laser. Typically, such control requires modifying the nanoparticle material, size, shape, separation, and extent of aggregation.

Optimizing plasmonic properties for SERS is not however as simple as matching the plasmon peak to the laser wavelength[24,25] because SERS depends on the optical near-field at the surface of the metallic nanostructure, whereas the plasmon resonance is usually measured by far-field optical properties such as scattering and extinction. The two are related but not necessarily in a straightforward way.[26] For example, individual spherical nanoparticles can show strong extinction but are poor SERS substrates since their plasmonic modes possess only a moderate near-field enhancement. In the case of nanoparticle assemblies, there will in general be redshifted coupled plasmon modes that confine light at the nanoparticle interstices, however, the details of how the near- and far-field relate are non-trivial. This relationship describes the basis of SERS and so understanding the details is essential if the SERS is to be analyzed, predicted, and optimized.

In this work, we study the relationship between the SERS response and the scattering properties of the plasmonic nanoarchitectures formed within microfluidic droplets by dark-field scattering spectroscopy and link to corresponding simulations. In order to generate nanoparticle assemblies, we make use of the macrocyclic molecule cucurbit[5]uril (CB[5]), which is known to precisely define the interparticle spacing on the nanometer scale.[27,28] This degree of control results in well-defined nanoparticle assemblies in which the plasmonic properties are governed by chains or chain-like subunits of nanoparticles.[29] In addition, the host–guest chemistry of cucurbit[n]uril allows analytes to be precisely placed in the SERS hot spots at the nanoparticle interstices.[30]

Microdroplets provide a well-controlled environment in which to study CB[5]-induced nanoparticle assembly. Using a microfluidic device, microdroplets are prepared and loaded with a mixture of CB[5] and gold nanoparticles (AuNPs). The nanoassembly progresses along the channel and so can be tracked on the millisecond timescale by inspecting successive spatial volumes. By this method, it is therefore possible to study precisely the relationship between the SERS and the optical properties of the nanoaggregate during the early stages of nanoparticle assembly. Our analysis provides new insights into the process of nanoassembly within microfluidic droplets, which is crucial for SERS optimization, for nanoparticle synthesis, and in working toward the guided assembly of individual nanostructures.

2. Results and Discussion

2.1. Refractive-Index-Matched Microdroplets

Nanoassembly of gold nanoparticles is studied inside water microdroplets (60 μm diameter) surrounded by oil, created in a standard microfluidics setup (**Figure 1**a, discussed below). When the gold nanoparticles bind together with carefully controlled gap spacing, new red-shifted coupled plasmon modes are produced. To characterize the evolving nanoassembly, we use dark-field spectroscopy as it is a sensitive background-free probe of these plasmon resonances. However, its application in microfluidics is hindered by strong reflections from the curved water-oil interfaces. In dark-field microscopy, samples are illuminated at higher incident angles than the objective lens collects, which suppresses direct reflections and picks out scatterers of the incident light. Dark-field spectroscopy is thus a subtle probe of nanostructures, but if the nanostructures have small volumes their signals can easily be swamped by any parasitic background. When illuminating microdroplets at high angles, the spherical interfaces redirect light into the detection directions, overwhelming any signal from nanoparticles. It is therefore necessary to match the refractive index of the oil and aqueous phases, which has not to our knowledge been previously attempted. This index matching is done through the calibrated addition of 1,3-bis(trifluoromethyl)-5-bromobenzene to the oil (see experimental section for detailed procedure).

Compared to microdroplets prepared with conventional oils, refractive-index-matched microdroplets are significantly
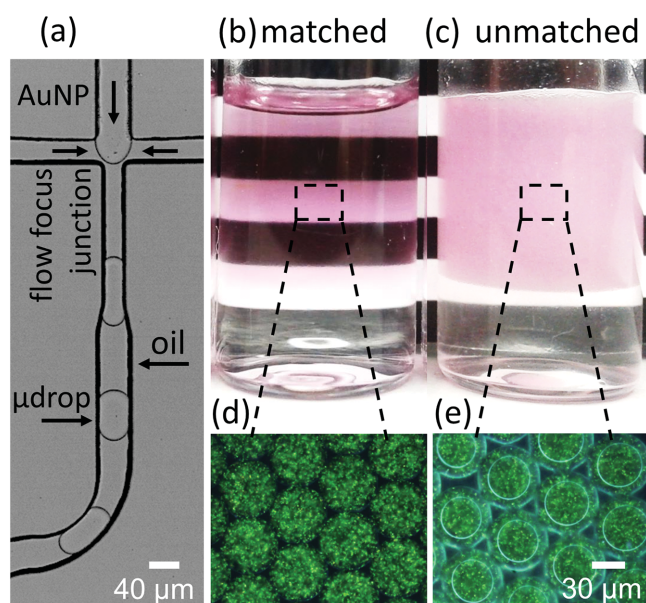
Figure 1. a) Bright-field image of microdroplet formation at a flow-focusing junction (top) with AuNP aqueous solution. b) Photo of collected microdroplets with refractive-index-matched oil and c) the same with conventional oil. d, e) Corresponding dark-field images of the emulsions in panels (b) and (c), respectively. The AuNPs are 86 ± 4 nm diameter and nonaggregated.

more transparent (Figure 1b,c). In this case, a pure nonaggregating dense AuNP suspension (each NP 86 ± 4 nm in diameter giving large scattering) is used within the microdroplets. This gives a speckled texture (Figure 1d,e) inside each microdroplet from the scattering of individual nanoparticles, of green hue due to the monomer dipolar plasmon mode (550 nm). In dark-field microscopy with the unmatched oil, two bright rings centered on each microdroplet are produced (Figure 1e). These rings correspond to the reflection of the high-incident-angle dark-field illumination from each microdroplet–oil

interface. By contrast, with the refractive-index-matched oil no substantial background is observed (Figure 1d).

The scattering intensity scales with r^6 (in the quasistatic approximation), r being the nanoparticle radius, and so the relatively large nanoparticles shown (86 ± 4 nm in diameter) represent a best case signal to background ratio. Even in this case, refractive index matching removes a background corresponding to ≈40% of the dark-field intensity.

2.2. Microfluidic AuNP Assembly

Water-in-oil microdroplets containing AuNPs are generated at a flow-focusing junction on a standard polydimethylsiloxane (PDMS)-glass microfluidic chip (Figure 1a). It is well established that this method can generate monodisperse microdroplets at up to kilohertz frequencies. Having suppressed the dark-field background it is possible to quantitatively study AuNP assembly in microdroplets by scattering spectroscopy. CB-AuNP assembly is triggered on chip by first combining an AuNP suspension (30 ± 6 nm diameter, final concentration ≈3 × 10¹¹ NP mL⁻¹) with a CB[5] solution (final concentration 450 × 10⁻⁶ M) and then forming microdroplets using a double flow-focus geometry (schematically shown in **Figure 2**a). Shear forces at the second flow focus junction segment the combined aqueous phase into monodisperse microdroplets in the surrounding refractive-index-matched oil. After formation, the microdroplets travel along a serpentine channel to ensure rapid mixing of the droplet contents by chaotic advection.[31] Complete mixing is achieved during the first channel corner (Figure S1, Supporting Information). Once the CB[5] and the AuNPs are mixed, the CB[5] binds the AuNPs together through interactions between the Au surface and the carbonyl groups of the CB portals.[27,32] The CB[5]:AuNP concentration ratio places the assembly in a diffusion-limited assembly regime (Figure S2, Supporting Information).
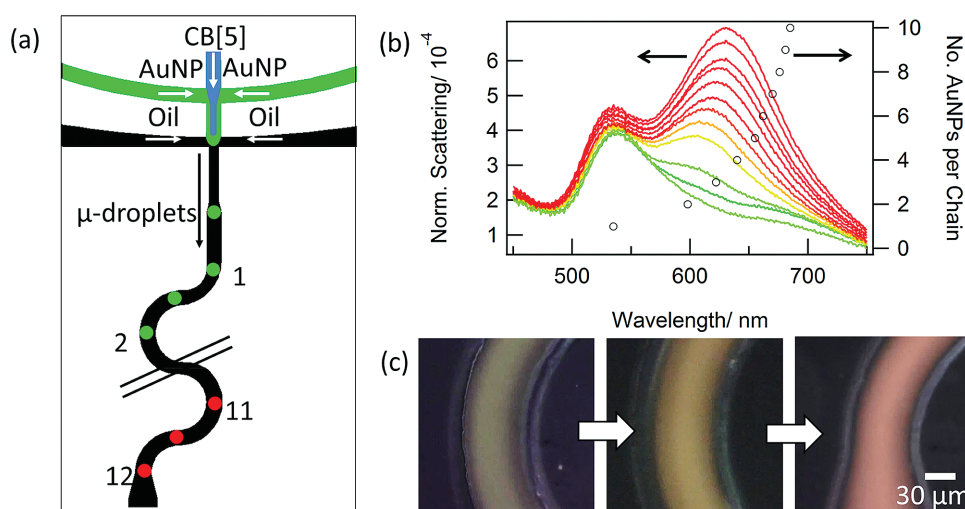

Figure 2. a) Schematic of microfluidic device used for microdroplet nanoparticle assembly experiments. Droplets flow along serpentine channel and are measured at sequential areas by dark-field spectroscopy indicated by numbered spots. Dark-field scattering spectra (normalized to a Lambertian scatterer) at these positions are plotted in panel (b), with a green to red color legend for the sequential areas 1, 2, etc. The wavelength of the scattering spectral maxima calculated for AuNP monomers, dimers, trimers, etc., are also indicated (open circles, length of each simulated chain on the right-hand axis). c) Dark-field images from the start, middle, and end of the serpentine channel.

In this arrangement, the flow of the droplet stream means that the time from the start of the nanoassembly is converted into spatial distance along the flow channel. Stages in the nanoassembly can therefore be analyzed by taking time-averaged measurements from different locations along the channel. This allows for millisecond resolution of the process of AuNP assembly without requiring millisecond integration times. From the flow rates and channel geometry, the total assembly time period on chip analyzed here is up to 110 ms.

Dark-field spectra of the microdroplet flow at sequential points along the channel (thus at increasing times separated by 10 ms from the initial mixing) clearly evolve rapidly (Figure 2b). With integration times of 20 s, each spectrum averages scattering from a few thousand microdroplets passing under the collection spot (40 μm diameter). Dark-field images taken along this channel (Figure 2c, 2 s exposures) show the green to red trend observed in the spectra, and also the increase in overall scattering intensity. The most prominent feature in the spectra besides the monomer mode at 540 nm is the progressive appearance of a longer wavelength "aggregate" mode, which is attributable to the formation of chain-like AuNP assemblies that support coupled plasmons. The coupled mode redshifts as the effective length of these chains increases.[29]

However, it should be noted that in this previous work the nanoparticle chains corresponded to optically active subunits embedded within larger nanoparticle clusters. Here, as we shall see, the early-stage assembly that the microfluidics make accessible enables us to study the optical behavior governed by short isolated chains (dimers, trimers, etc.) rather than cluster subunits. In this regime, it is appropriate to model the structures themselves as chains for two main reasons. First, it has been previously shown that the optical response is insensitive to chain kinking and so even quite disordered structures are optically chain-like.[29] Second, in the early stages of assembly the number of possible aggregate configurations is limited. The only possible configuration of a nanoparticle dimer is a straight two-membered chain. For a trimer a trigonal geometry is possible, but in diffusion-limited aggregation (discussed in detail below) it is much more likely that a three-membered chain is formed, either straight or kinked. Comparison of the resonant wavelengths from experiment with simulated nanoparticle chains of increasing length indicates that the active chains are only a few nanoparticles long (Figure 2b).

These simulations use the boundary element method (BEM)[33] to characterize linear chains of spherical 30 nm diameter AuNPs with an interparticle gap of 1.4 nm. Using commercial citrate-capped AuNPs (BBI solutions) with CB[5], we always find 0.9 nm gaps (confirmed by measuring the dimer mode wavelengths for a range of AuNP diameters in extinction spectroscopy, Figure S3 in the Supporting Information). Here, using citrate-capped AuNPs made in-house in which surfactants can be entirely controlled, we instead find fixed ≈1.4 nm gaps (Supporting Information). This could correspond to separations of two stacked CBs (as has been seen previously)[34] and shows the sensitive control required of the surface chemistries and ionic strength. These verified ≈1.4 nm gap sizes are then used in the simulations.

Diffusion-limited colloidal aggregation (DLCA) kinetics[35] also predicts that for this AuNP concentration and timescale the assembly will be in the dimer/trimer formation regime (**Figure 3**). In outline, DLCA kinetics assumes that all collisions of monomers and/or clusters result in irreversible binding of those particles together. Thus, the only factors determining the rate of aggregation are the particle concentrations and the particle diffusion rates. The cluster-size distribution is determined by the collision rates of every cluster type with every other cluster type according to the Smoluchowski rate equations. For example, the number of monomers depends on the rate of collision of monomers with other monomers (to form dimers), with dimers (to form trimers), with trimers (to form quadrumers), and so on. The seminal paper by Lin et al. describes the solution for the cluster-size distribution that is used here (also see the Experimental Section).[35]

In this regime, DLCA kinetics is only approximate because it assumes that the diffusion rate of the cluster is determined by its fractal dimension. This assumption is unreliable for small clusters that, unlike large aggregates, are not quasi-fractal. Nonetheless, simulated scattering spectra for the resulting population distributions (see methods) show a good match to the experimental spectra (Figures 2b and 3b). Although the
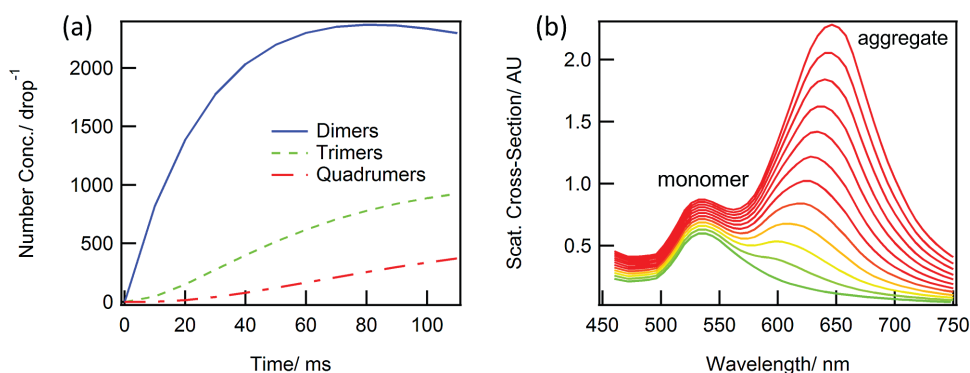

Figure 3. a) AuNP cluster distributions during the microdroplet AuNP assembly according to diffusion-limited colloidal aggregation kinetics.[35] At $t = 0$, the number of monomers per drop is set to 16 000. b) Simulated time-resolved scattering cross sections for the population distributions in panel (a), calculated from the scattering cross section for simulations of single monomers, dimers, etc., weighted according to their population distributions.
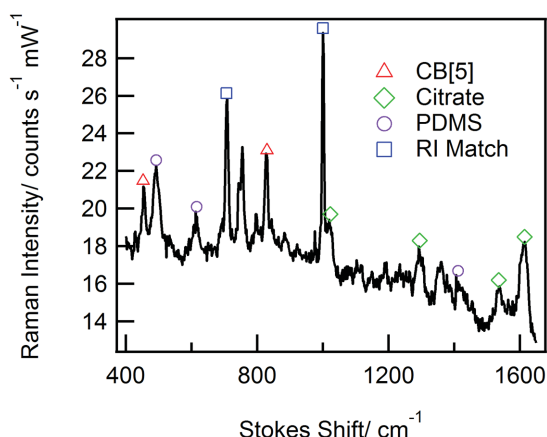
Figure 4. Raman spectrum from point 11 (Figure 2a) near the end of the serpentine channel. SERS peaks marked are from the cucurbit[5] uril linker molecule and citrate as well as background signals from the oil (RI Match) and the PDMS encapsulation.

Table 1. Frequencies and assignments for the experimental Raman spectral lines (Figures 4 and 5), where v, stretch; β, bend; and σ, scissor.

Label	Stokes shift [cm^{-1}]	Assignment	Ref
CB1	452	CB[5], σNCN	[36]
CB2	829	CB[5], δCNC+ ρCH2	[36]
C1	1023	Citrate, vCCO, trans	[37]
C2	1295	Citrate, vCO+ δOH	[37]
C3	1535	Citrate	[37]
C4	1614	Citrate, vCOO, asym	[37]
P1	490	PDMS, vSiOSi	[38]
P2	617	PDMS	[38]
P3	1411	PDMS, βCH3	[38]
O1	706	RI matching oil	
O2	1000	RI matching oil	
B	N/A	SERS Background	

wavelength of the simulated "aggregate" mode is 16 nm red-shifted relative to the experimental mode, this small shift can result from several factors, including the disorder of the experimental chains,[29] the exact value of the interparticle gap, and the known limitations of the DLCA kinetic model.

The relative intensities of the aggregate and "monomer" modes (the short wavelength mode including also transverse chain modes) differ between experiment and simulation, which points to a possible excess of monomers in the experiments with respect to the prediction from DLCA kinetics. From the modeling perspective, the difference may also be sensitive, for example, to having accounted for the random chain orientations by a simple weighting of the polarizations perpendicular and parallel to the chain axis (see the Experimental Section). Nevertheless, overall our modeling allows the identification of the evolution of monomer, dimer, and trimer populations with time in experiment.

2.3. Microfluidic SERS

In order to examine the effect of the emerging plasmon modes on SERS, Raman spectroscopy is performed on the same microfluidic system in the same locations examined by dark-field spectroscopy. A 633 nm laser is used for Raman excitation that is resonant with the plasmon modes that emerge along the channel (Figure 2b). Measurements are again averaged over the microdroplet flow (integration times of 10 s). The resulting Raman spectra show clear vibrational peaks from the CB[5] linker molecule, citrate (which initially caps the AuNPs), and background peaks from the surrounding (RI-matched) oil and the PDMS device (**Figure 4**, **Table 1**).

Both the focus depth and the position along the channel affect the amplitude of the SERS spectra. To characterize these variations, depth series spectra (z-resolution $\approx$5 μm) are recorded at each location (**Figure 5**a). In each case a spline fit is used to subtract the SERS background, which is also plotted. While each component has a different Raman amplitude (Figure 4), these are normalized in Figure 5 to

best compare their depth profiles. At the advanced stage of assembly (point 11, in Figure 5a) the strong SERS from the CB:Au aggregates is clearly maximized in the vertical center of the channel between the glass and PDMS walls, due to the larger volume of the microdroplets passing through this plane.

From this analysis, the intensity of the Raman lines at each location along the channel is tracked (Figure 5b), taking the maximum SERS (in z) for each component after background subtraction, and normalizing them to allow easy comparison of their evolution during aggregation. Two different characteristic behaviors are observed depending on the type of spectral peak (which also confirms the Raman assignments given). The peaks associated with the oil (and the PDMS) are not surface enhanced and thus not dependent on the AuNP aggregation state, hence remaining constant along the channel (blue points). In contrast, the CB lines (red) are plasmonically enhanced and so increase in intensity with aggregation time. The SERS background (that behaves as a broad pseudofluorescence always accompanying plasmon-enhanced SERS)[39] also increases slightly along the channel.

In order to directly correlate the SERS to the emergence of the plasmonic mode, we plot the Raman intensity of the SERS-active CB lines against the scattering at 633 nm, which is the excitation wavelength of the Raman laser (**Figure 6**). For the experimental data, the Raman signal is processed as above and the scattering taken from the corresponding dark-field spectra (Figure 2b). The simulated data is for the DLCA population distribution described in Figure 3. At our concentrations, aggregates are many microns apart and both scattered fields and Raman signal are summed incoherently (see the Experimental Section). For both simulated and experimental data, reference spectra at $t = 0$ (before aggregation) are subtracted to remove "monomer" modes from the dark-field scattering signal. This subtraction will be critical for the ensuing interpretation of the results.

As the scattering intensity of the plasmonic mode increases so does the SERS. While related correlations have been observed elsewhere,[40–42] and a polynomial relationship between nanoparticle cluster size and the SERS intensity has been suggested,[43] there is no universal relationship
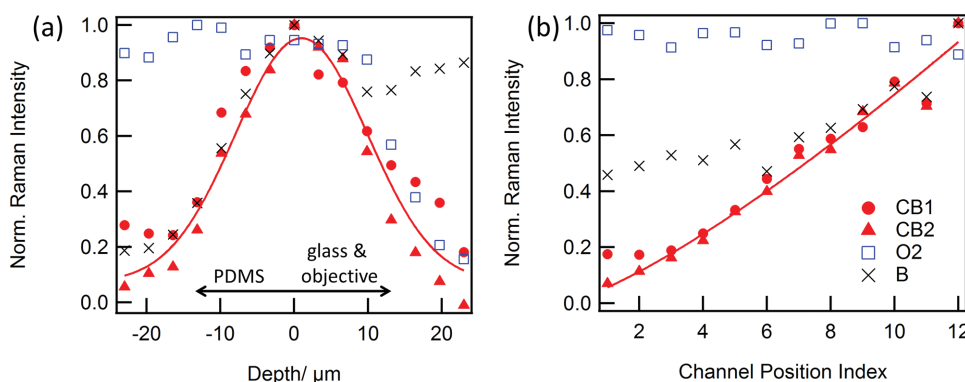
Figure 5. Combined legend refers to Table 1. a) Normalized SERS intensities versus confocal collection depth ($z = 0$ is channel center) at point 11 near the serpentine channel end (Figure 2a). Arrow shows limits of the channel. b) Normalized Raman intensity at increasing time, corresponding to a position along the channel (at points in Figure 2a).

between far-field optical properties (such as scattering) and SERS.[24,25] However, as a result of the very short timescales we are able to investigate here, the nanoassembly is in a regime dominated by dimer and trimer formation (Figure 3a), which enables much simpler interrogation of the correlation between SERS and scattering.

The SERS signal predominantly originates from nanoparticle gaps and is much weaker for monomers. Thus, for small numbers of trimers and larger chains, the SERS signal should be directly proportional to the number of dimers. Similarly, the contribution of the monomers (and transverse modes) to the scattering signal at 633 nm should be weak because this wavelength lies outside the single nanoparticle resonance and because the subtraction of the $t = 0$ signal partially suppresses this contribution. The measured scattering should thus also be approximately proportional to the number of dimers, and thus a simple relationship SERS $\propto$ Scat at the examined wavelength is expected, particularly at the beginning of aggregation when chains of three or more spheres are rarer (at early times corresponding to bottom left of Figure 6).
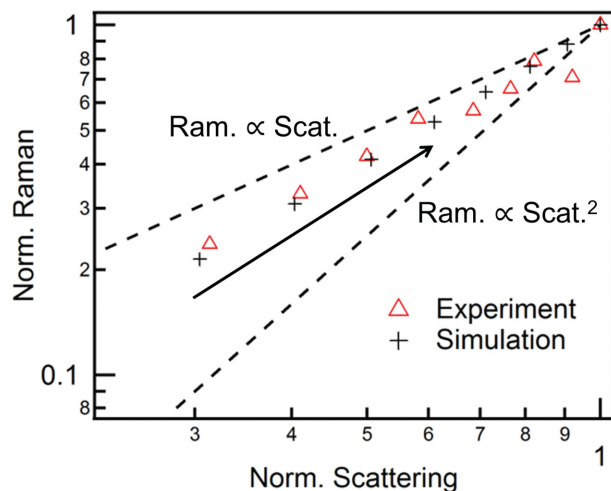
Experimentally, we find SERS $\propto$ Scat$^{1.2}$. The small difference from the ideal linearity can be explained by the population of larger chains (and also by non-perfect suppression of the background or of contributions from the monomer). Notably, the dependence of SERS with scattering becomes rather complicated when comparing simulated chains of different lengths (Figure S4, Supporting Information), and we have also previously seen complex relationships between extinction and SERS.[27] This is in contrast to the simple correlation observed here in the limit of short chains.

We can reproduce these experimental results with our calculations for the chain length distribution in Figure 3a. The calculated results in Figure 6 show an excellent match consistent with SERS $\propto$ Scat$^{1.2}$. The agreement supports our interpretation of the quasi-linear relationship coming from a distribution of short chains (mostly monomers or dimers) and is consistent with the expectation from DLCA kinetics.

More generally, this interpretation is valuable for the optimization of SERS in nanoparticle assemblies. The near-linear relationship between SERS and scattering confirms that SERS arises from the nanoparticle gaps. As aggregation takes place the number of gaps increases and so does the SERS. However, there are at least two caveats. First, the number of effective gaps will saturate for large aggregates because in a fractal structure not all of the gaps are active. For our nanoparticles and interparticle spacer, this occurs when the optical chain length is around 10–16 nanoparticles long.[27,29] Second, during aggregation the wavelength of the coupled plasmonic mode redshifts (Figure 2b). As this mode shifts to the red side of the laser line, the surface enhancement will drop (see Figure S4a, Supporting Information).

Figure 6. Normalized Raman and scattering at 633 nm from both experiment and simulations. Data extracted from Figure 2b and simulations from DLCA nanoparticle aggregate distributions. The strong and SERS-active 829 cm^{-1} line of CB[5] (CB2) is used for the Raman.

2.4. Few-AuNP Microdroplets

So far the case of relatively high AuNP concentrations has been studied, with $\approx$16 000 AuNPs per microdroplet. Microdroplet AuNP nanoassembly in this regime, while of much interest for sensing and analysis, supports an assembly process similar to bulk aggregation. However if the nanoparticle concentration is reduced further, then the assembly process is highly distinct from bulk aggregation because the aggregate
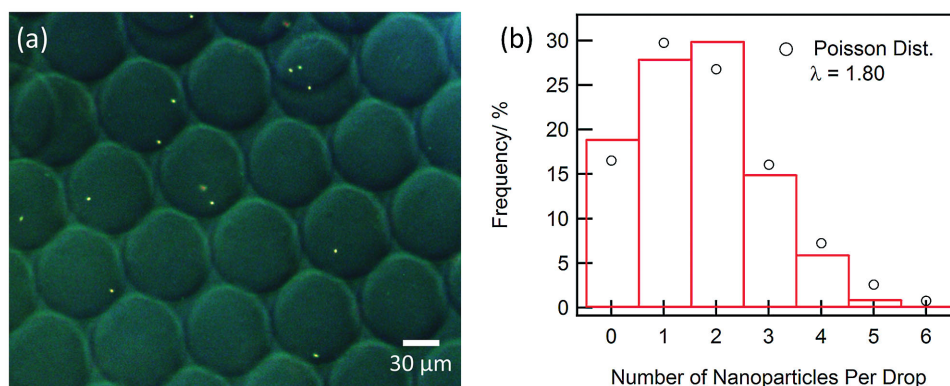
Figure 7. a) Dark-field image of microdroplets containing small numbers of 138 ± 5 nm diameter AuNPs. The refractive index is deliberately slightly mismatched, so that droplet boundaries can be clearly seen. No CB[5] aggregant is used here, and so the bright points correspond to individual AuNPs. By scanning the focus vertically, the full droplets can be inspected and the nanoparticle loading can be directly determined. b) Number of nanoparticles per drop, compared to Poisson distribution of average loading $\lambda = 1.8$ NPs per drop.

size becomes limited by the number of nanoparticles in the full microdroplet volume. Although conventional, diffusion-limited or reaction-limited aggregation is also limited by the number of particles (a 0.5 mL cuvette of AuNPs at typical concentrations contains $\approx 10^{10}$ AuNPs), in practice sedimentation takes place well before this limit is reached. We term this limit number-limited colloid aggregation (NLCA). Particularly interesting is the "digital" case where there are only a few AuNPs per microdroplet.

Random insertion of nanoparticles into microdroplets yields a number distribution which follows Poisson statistics, and so specific numbers of AuNPs can be isolated in relatively high yields. For instance, as a proportion of the initial AuNPs, two nanoparticles can be isolated in a yield of 31% (**Figure 7**). Although dimers are not prepared here, for comparison the highest AuNP dimer yield in the literature (to our knowledge) is 26%.[44] We note that there are several reports of higher "yields" than 26%,[45,46] however, this arises from inconsistent terminology. Here we use "yield" in the sense it is used in chemistry (the proportion of AuNP monomers converted to dimers) as opposed to purity (proportion of dimers in isolated product).

A further intriguing possibility is isolating specific numbers of nanoparticles in each droplet, such that every droplet contains, for example, two particles. This would require ordering the particle injection process as has been done geometrically for microparticles.[47] DNA molecules have also been injected one by one into microdroplets.[48] For plasmonic nanoparticles it is now conceivable that optical, electrical, or hydrodynamic forces could be used to induce such ordering and give controlled encapsulation, allowing investigation of different aggregation regimes (NLCA) and producing controlled NP aggregate sizes tuned to specific wavelengths.

3. Conclusion

Microfluidic microdroplets are of substantial interest for the creation of plasmonic structures and for reproducible SERS-based sensing. However, this field has been hindered by the lack of tools to characterize plasmonic properties on-chip. Here, enabled by a novel refractive-index-matched microdroplet formulation, we show that the nanoparticle assembly process can be directly monitored in microfluidic droplets by dark-field spectroscopy. The microdroplets provide rapid mixing of the AuNPs and a CB[5] molecular glue, while the flow spatially separates the assembly process on-chip. We show that this provides sufficiently high time resolution to identify and precisely study the early stages of nanoparticle assembly. In particular in this initial regime, dimer formation dominates the optical properties, which results in a near-linear proportionality between the evolving dark-field scattering and SERS intensities, on the condition that monomer scattering contributions are suppressed. This work thus provides a strong basis from which to characterize plasmonic structures in microfluidic droplets, for example, in nanoparticle synthesis and to develop SERS applications. We also show that microdroplets can be used to isolate small numbers of nanoparticles in relatively high yields, which can allow the assembly and dynamic study of few nanoparticle structures.

4. Experimental Section

Microfluidics: PDMS microfluidic devices were made by a standard soft lithography procedure.[49] Briefly, PDMS was cast on SU8 masters (made by UV photolithography) and cured at 70 °C overnight. The PDMS was then peeled off the master, holes were punched for the inlets/outlets, and then the PDMS was plasma bonded to glass coverslips. In order to make the microchannels fluorophilic, they were then functionalized by flowing a freshly prepared solution of trichloro(1H,1H,2H,2H-perfluorooctyl)silane (Alfa Aesar, 0.5 v/v% in FC40) through the channels, allowing to stand for 5 min, and then flushing through with nitrogen. Flow was driven using New Era syringe pumps (NE-1000, NE-4002x) with 1 mL plastic syringes (NORM-JECT). The flow rates were set at 100 μL h^{-1} for the oil and 200 μL h^{-1} for the combined aqueous phase. High aqueous flow rates (relative to the overall flow rate) were used to minimize the background signals from the oil.

Refractive Index Matching: Reformulating the known equations for the refractive indices of mixtures,[50] the volume fractions

of each component in a mixture necessary to achieve a desired refractive index, n_{mix}, could be derived. In the case of a two-component system, the required volume fraction of one of the components, φ_1, is given as

$$\varphi_1 = \frac{\rho_2(n_{mix} - n_2)}{\rho_2(n_{mix} - n_2) + \rho_1(n_1 - n_{mix})} \quad (1)$$

where n_i and ρ_i ($i = 1,2$) are the refractive indices and densities of the ith components, respectively. By definition, $\varphi_2 = 1 - \varphi_1$. Using Equation (1), the refractive index of the oil phase (Pico-Surf 2, 5 wt% in FC40, Dolomite, $n = 1.290$) was matched to that of water ($n = 1.333$) by adding 1,3-bis(trifluoromethyl)-5-bromobenzene (Sigma-Aldrich, $n = 1.427$) at 33.2 v/v% to the oil. The refractive index dispersion and temperature dependence were not substantial enough to require consideration for this application. It is also noted that the ability to do microdroplet sorting by conventional methods would not be impaired by this combination, as the index matching is done at optical frequencies, not at the lower frequencies used for dielectrophoresis.

In order to select a suitable index-matching solvent, a range of benzene-based compounds (for relatively high refractive index) with fluorocarbon substituents (for miscibility with oil) was trialed. These included: 3-bromobenzenetrifluoride; 1,1,1-trifluorotoluene, 1-bromo-4-fluorobenzene; 1,3-bis(trifluoromethyl) benzene; and 1,3-bis(trifluoromethyl)-5-bromobenzene. The latter was found to match the miscibility criterion, not to interfere with droplet formation, and also to have a low odor.

Nanoparticle Synthesis: 30 nm diameter AuNPs were made by a modified Turkevich procedure. Briefly, in this Turkevich protocol, trisodium citrate (0.73 mL, 152 mM) was added (quickly, in one portion) to a rapidly stirring and vigorously boiling solution of chloroauric acid (149.9 mL, 0.38×10^{-3} M). The solution was refluxed for 10 min and then allowed to cool to room temperature. This yielded 30 ± 6 nm diameter AuNPs. These were concentrated by a factor of 10 by centrifugation followed by redispersion in a portion of the supernatant. The solutions/suspensions are aqueous throughout. Larger nanoparticles were made following the method reported by Ziegler and Eychmuller.[51]

Microscopy and Spectroscopy: Dark-field microscopy was performed on an Olympus IX71 inverted microscope modified for reflected dark-field illumination and equipped with a 20x objective (Olympus MPLFLN20xBD, N.A. 0.45). For dark-field spectroscopy, a 600 µm core optical fiber (Ocean Optics QP600-2-VIS-NIR) was coupled in a conjugate focal plane and attached to a spectrometer (Ocean Optics QE65000) such that spectra could be taken from well-defined spatial regions of the dark-field image ≈40 µm in diameter. The tungsten−halogen lamp of the microscope (spectral range: 400−900 nm) was used as the light source and spectra were normalized by a white light reflectance standard (Lab-sphere Spectralon SRM-99). Spectra were also background subtracted at each point, to remove the slight scattering signals from the microfluidic device (channel walls, dust, etc.).

Raman spectroscopy was performed using a Renishaw inVia confocal Raman microscope using a 100× objective (Leica N PLAN EPI 100×, N.A. 0.85) in the backscattering geometry. The acquisition time was 10 seconds with a 1200 lines mm^{-1} grating to give a spectral resolution of < 4 cm^{-1}. Illumination was from a 633 nm HeNe laser (10 mW at sample). Scanning the confocal collection depth at each location corrects for the slight variations in channel depth. The Raman background was fit using a spline for background subtraction.

AuNPs were characterized by scanning transmission electron microscopy (Hitachi S-5500), with mean diameters and standard deviations given from a minimum of 50 measurements.

DLCA Kinetics: Following Lin et al. the cluster mass distribution during DLCA is given by[35]

$$N(M) = \frac{N_0}{\bar{M}^2}\left(1 - \frac{1}{\bar{M}}\right)^{M-1}$$

where $N(M)$ is the number of clusters of mass M and N_0 is the number of particles. It is convenient to calculate in particle mass units, so that a monomer is of mass 1, a dimer of mass 2, etc. $\bar{M}$ is defined as

$$\bar{M} = \frac{t_a}{t_0} + 1$$

where t_a is the aggregation time point and

$$t_0 = \frac{3\eta V}{8k_B T N_0},$$

with particle concentration $\frac{N_0}{V}$, viscosity η, Boltzmann constant k_B, and temperature T.

Simulations: The theoretical response of straight chains of metallic spheres was calculated using the BEM.[33] Scattering cross sections were calculated for linear chains of identical gold nanoparticles in water (permittivity 1.77) with an interparticle separation of 1.4 nm and diameter 30 nm. The incident light was a plane wave with wavevector perpendicular to the chain axis. Unpolarized spectra were built from polarized simulations as $\frac{2}{3}s\text{-pol} + \frac{1}{3}p\text{-pol}$ where s-pol and p-pol are the spectra for the electric field polarized perpendicular and parallel to the chain axis, respectively. A standard size correction was used for the permittivity of gold in Johnson and Christy.[29,52,53]

The Raman enhancement at each gap was obtained as the square of the electric field enhancement at the gap center and at the illumination frequency multiplied by the corresponding value at the emission frequency (Stokes shift 826 cm^{-1}). The obtained Raman enhancement is added incoherently over all gaps. Both scattering and Raman calculations add incoherently the result from the different lengths weighted according to the chain length distribution in Figure 3a.

Supporting Information

Supporting Information is available from the Wiley Online Library or from the author. Open access source data can be found at: https://www.repository.cam.ac.uk/handle/1810/253505.

Acknowledgments

[1] E. C. Le Ru, E. Blackie, M. Meyer, P. Etchegoin, *J. Phys. Chem. C* **2007**, *111*, 13794.

[2] K. Bosnick, M. Maillard, L. Brus, *J. Phys. Chem. B* **2003**, *107*, 9964.

[3] S. Nie, S. R. Emory, *Science* **1997**, *275*, 1102.

[4] K. Kneipp, Y. Wang, H. Kneipp, L. T. Perelman, I. Itzkan, R. R. Dasari, M. S. Feld, *Phys. Rev. Lett.* **1997**, *78*, 1667.

[5] J. Kim, *Lab Chip* **2012**, *12*, 3611.

[6] T.-A. Meier, R. J. Beulig, E. Klinge, M. Fuss, S. Ohla, D. Belder, *Chem. Commun.* **2015**, *51*, 8588.

[7] A. Walter, A. März, W. Schumacher, P. Rösch, J. Popp, *Lab Chip* **2011**, *11*, 1013.

[8] X. Niu, A. J. DeMello, *Biochem. Soc. Trans.* **2012**, *40*, 615.

[9] C. D. Syme, C. Martino, R. Yusvana, N. M. S. Sirimuthu, J. M. Cooper, *Anal. Chem.* **2012**, *84*, 1491.

[10] M. P. Cecchini, J. Hong, C. Lim, J. Choo, T. Albrecht, A. J. DeMello, J. B. Edel, *Anal. Chem.* **2011**, *83*, 3076.

[11] K. R. Ackermann, T. Henkel, J. Popp, *ChemPhysChem* **2007**, *8*, 2665.

[12] R. Gao, N. Choi, S.-I. Chang, S. H. Kang, J. M. Song, S. I. Cho, D. W. Lim, J. Choo, *Anal. Chim. Acta* **2010**, *681*, 87.

[13] E. Kämmer, K. Olschewski, T. Bocklitz, *Phys. Chem. Chem. Phys.* **2014**, *16*, 9056.

[14] B. Liu, W. Jiang, H. Wang, X. Yang, S. Zhang, Y. Yuan, T. Wu, Y. Du, *Microchim. Acta* **2013**, *180*, 997.

[15] E. Kämmer, K. Olschewski, P. Rösch, K. Weber, D. Cialla-May, J. Popp, *J. Raman Spectrosc.* **2015**, DOI: 10.1002/jrs.4849.

[16] A. März, T. Henkel, D. Cialla, M. Schmitt, J. Popp, *Lab Chip* **2011**, *11*, 3584.

[17] S. Duraiswamy, S. A. Khan, *Small* **2009**, *5*, 2828.

[18] S. Duraiswamy, S. A. Khan, *Nano Lett.* **2010**, *10*, 3757.

[19] S. Abalde-Cela, B. Auguié, M. Fischlechner, W. T. S. Huck, R. A. Alvarez-Puebla, L. M. Liz-Marzán, C. Abell, *Soft Matter* **2011**, *7*, 1321.

[20] J. Zhang, R. J. Coulston, S. T. Jones, J. Geng, O. A. Scherman, C. Abell, *Science* **2012**, *335*, 690.

[21] A. Theberge, F. Courtois, Y. Schaerli, M. Fischlechner, C. Abell, F. Hollfelder, W. Huck, *Angew. Chem., Int. Ed. Engl.* **2010**, *49*, 5846.

[22] A. Huebner, S. Sharma, M. Srisa-Art, F. Hollfelder, J. B. Edel, A. J. Demello, *Lab Chip* **2008**, *8*, 1244.

[23] Y. Zhu, Q. Fang, *Anal. Chim. Acta* **2013**, *787*, 24.

[24] M. Moskovits, *Phys. Chem. Chem. Phys.* **2013**, *15*, 5301.

[25] E. C. Le Ru, C. Galloway, P. G. Etchegoin, *Phys. Chem. Chem. Phys.* **2006**, *8*, 3083.

[26] P. Alonso-González, P. Albella, F. Neubrech, C. Huck, J. Chen, F. Golmar, F. Casanova, L. E. Hueso, a. Pucci, J. Aizpurua, R. Hillenbrand, *Phys. Rev. Lett.* **2013**, *110*, 1.

[27] R. W. Taylor, T.-C. Lee, O. A. Scherman, R. Esteban, J. Aizpurua, F. M. Huang, J. J. Baumberg, S. Mahajan, *ACS Nano* **2011**, *5*, 3878.

[28] T.-C. Lee, O. A. Scherman, *Chem. Commun.* **2010**, *46*, 2438.

[29] R. Esteban, R. W. Taylor, J. J. Baumberg, J. Aizpurua, *Langmuir* **2012**, *28*, 8881.

[30] S. Kasera, F. Biedermann, J. J. Baumberg, O. A. Scherman, S. Mahajan, *Nano Lett.* **2012**, *12*, 5924.

[31] H. Song, M. R. Bringer, J. D. Tice, C. J. Gerdts, R. F. Ismagilov, *Appl. Phys. Lett.* **2003**, *83*, 4664.

[32] Q. An, G. Li, C. Tao, Y. Li, Y. Wu, W. Zhang, *Chem. Commun.* **2008**, *17*, 1989.

[33] F. García de Abajo, A. Howie, *Phys. Rev. Lett.* **1998**, *80*, 5180.

[34] T. C. Lee, O. A. Scherman, *Chem. Eur. J.* **2012**, *18*, 1628.

[35] M. Y. Lin, H. M. Lindsay, D. A. Weitz, R. Klein, R. C. Ball, P. Meakin, *J. Phys.: Condens. Matter* **1990**, *2*, 3093.

[36] S. Mahajan, T.-C. Lee, F. Biedermann, J. T. Hugall, J. J. Baumberg, O. A. Scherman, *Phys. Chem. Chem. Phys.* **2010**, *12*, 10429.

[37] V. H. S. de Melo, V. M. Zamarion, K. Araki, H. E. Toma, *J. Raman Spectrosc.* **2011**, *42*, 644.

[38] D. Cai, A. Neyer, R. Kuckuk, H. M. Heise, *J. Mol. Struct.* **2010**, *976*, 274.

[39] J. T. Hugall, J. J. Baumberg, *Nano Lett.* **2015**, *15*, 2600.

[40] J. C. Fraire, L. a Pe, E. a Coronado, *J. Phys. Chem. C* **2013**, *117*, 23090.

[41] A. Lee, G. F. S. Andrade, A. Ahmed, M. L. Souza, N. Coombs, K. Liu, R. Gordon, A. G. Brolo, E. Kumacheva, *J. Am. Chem. Soc.* **2011**, *133*, 7563.

[42] C. J. Addison, A. G. Brolo, *Langmuir* **2006**, *22*, 8696.

[43] C. P. Shaw, M. Fan, C. Lane, G. Barry, A. I. Jirasek, A. G. Brolo, *J. Phys. Chem. C* **2013**, *117*, 16596.

[44] L. Piantanida, D. Naumenko, M. Lazzarino, *RSC Adv.* **2014**, *4*, 15281.

[45] V. V Thacker, L. O. Herrmann, D. O. Sigle, T. Zhang, T. Liedl, J. J. Baumberg, U. F. Keyser, *Nat. Commun.* **2014**, *5*, 3448.

[46] H. Cha, J. H. Yoon, S. Yoon, *ACS Nano* **2014**, *8*, 8554.

[47] A. R. Abate, C.-H. Chen, J. J. Agresti, D. A. Weitz, *Lab Chip* **2009**, *9*, 2628.

[48] A. P. Ivanov, P. Actis, P. Jo, J. B. Edel, D. Klenerman, Y. Korchev, *ACS Nano* **2015**, *9*, 3587.

[49] D. C. Duffy, J. C. McDonald, O. J. Schueller, G. M. Whitesides, *Anal. Chem.* **1998**, *70*, 4974.

[50] J. Z. Sun, M. C. E. Erickson, J. W. Parr, *Int. J. Cosmet. Sci.* **2005**, *27*, 253.

[51] C. Ziegler, A. Eychmuller, *J. Phys. Chem. C* **2011**, *115*, 4502.

[52] L. B. Scaffardi, J. O. Tocho, *Nanotechnology* **2006**, *17*, 1309.

[53] P. B. Johnson, R. W. Christy, *Phys. Rev. B* **1972**, *6*, 4370.